

Improving the imaging capability of an on-axis transmission Kikuchi detector

Alice Bastos S. Fanta^{a,*}, Adam Fuller^a, Hossein Alimadadi^{a,c}, Matteo Todeschini^{a,e}, Daniel Goran^b, Andrew Burrows^{a,d}

^a DTU Nanolab, National Centre for Nano Fabrication and Characterization, Technical University of Denmark, Fysikvej 307, 2800 Kgs. Lyngby, Denmark

^b Bruker Nano GmbH, Berlin, Germany

^c Danish Technological Institute, Kongsvang Alle 29, 8000 Aarhus C, Denmark

^d ISS Group Services Ltd, Pellowe House, Francis Road, Withington, Manchester, Greater Manchester M20 4XP, UK

^e Blue Scientific Ltd., St. John's Innovation Centre, Cowley Road, Cambridge CB4 0WS, UK

ARTICLE INFO

Keywords:

Transmission Kikuchi Diffraction (TKD)
Orientation mapping
Correlative TKD and STEM images
In-situ analysis
Time resolved experiments

ABSTRACT

Transmission Kikuchi Diffraction (TKD) in the scanning electron microscope has been developing at a fast pace since its introduction less than a decade ago. The recently presented on-axis detector configuration, with its optimized geometry, has significantly increased the signal yield and facilitated the acquisition of STEM images in bright field (BF) and dark field (DF) mode, in addition to the automated orientation mapping of nanocrystalline electron transparent samples. However, the physical position of the integrated imaging system, located outside the detector screen, requires its movement in order to combine high resolution STEM images with high resolution orientation measurements. The difference between the two positions makes it impossible to acquire optimal signals simultaneously, leading to challenges when investigating site-specific nanocrystalline microstructures. To eliminate this drawback, a new imaging capability was added at the centre of the on-axis TKD detector, thus enabling acquisition of optimal quality BF images and orientation maps without detector movement. The advantages brought about by this new configuration are presented and the associated limitations are discussed.

1. Introduction

Transmission Kikuchi diffraction experiments in the SEM are carried out in two geometric distinct configurations. The first configuration, “off-axis” is where a standard EBSD detector is employed to collect transmitted Kikuchi patterns from an electron transparent specimen (often tilted) [1]. The second configuration, “on-axis” is where the head of the EBSD detector is replaced with a specially designed head to acquire the TKD patterns from directly underneath an electron transparent sample. In this configuration, the detector is positioned horizontally so that the optical axis of the electron column intersects the centre of the detector screen, hence the name, “on-axis TKD”.

The on-axis TKD configuration was first introduced by Fundenberger et al. [2] and commercialized by Bruker [3]. A comparison between the two configurations [4,5] reveals that due to the optimised position of the on-axis detector, lower beam currents and faster measurements are possible [4,5], while in terms of spatial and angular

resolution, only a small improvement was observed [5]. To the authors' knowledge, a comparison between the two configurations, in terms of its application in combination with EDS, is still lacking. However, TKD in combination with EDS has been demonstrated previously [6–10]. The biggest drawback of using a standard EDS detector to analyse electron transparent samples is the low count rate and related slow acquisition speed. Solutions to significantly improve the EDS acquisition speed and bring it to levels similar to on-axis TKD acquisition rates are commercially available, but they have yet to be explored extensively.

In terms of applications of TKD for materials characterization, most studies have used the standard off-axis detector configuration, as it has the advantage that no hardware modification is required. Nevertheless, interest in the on-axis configuration is rising due to the increased signal yield. Recent investigations on the depth resolution of on-axis TKD [11] and on the range of diffraction contrast depending on sample and microscope parameters for on-axis TKD have been presented [12].

* Corresponding author.

E-mail addresses: alice.fanta@cen.dtu.dk (A.B.S. Fanta), adam.fuller@cen.dtu.dk (A. Fuller), hoal@teknologisk.dk (H. Alimadadi), Daniel.Goran@bruker.com (D. Goran).

<https://doi.org/10.1016/j.ultramic.2019.112812>

Received 21 January 2019; Received in revised form 30 June 2019; Accepted 7 July 2019

Available online 08 July 2019

0304-3991/ © 2019 Elsevier B.V. All rights reserved.

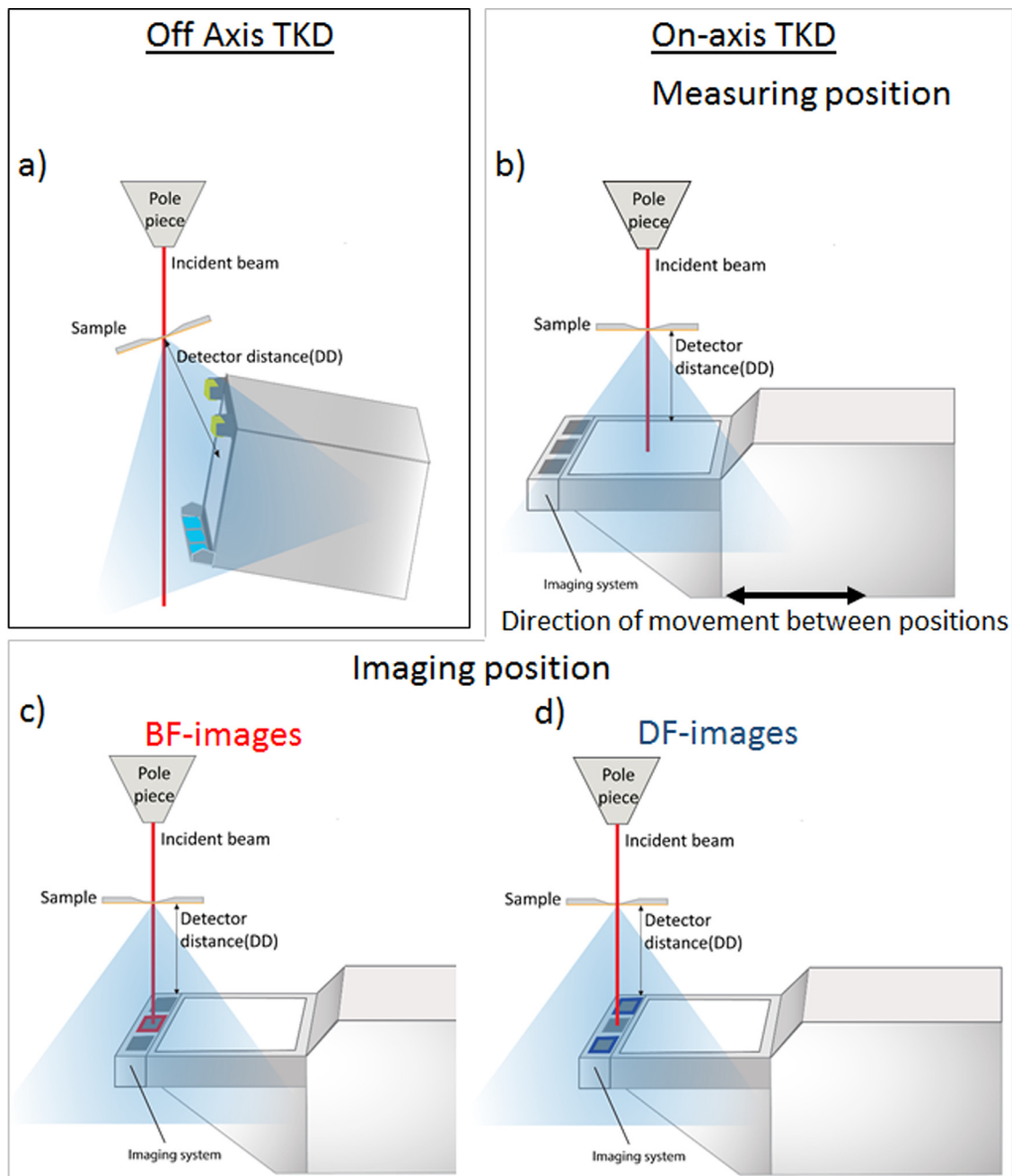


Fig. 1. Schematic representation of diffraction pattern detector configuration and imaging system. (a) Off-axis configuration with imaging system located above and below the phosphor screen. (b) On-axis TKD configuration in the measuring position with three imaging diodes located besides the phosphor screen. (c) On-axis detector configuration in the bright field imaging position, where only the diode located in the path of the direct beam is selected. (d) On-axis detector configuration in dark field imaging position, where the diodes located outside the path of the direct beam (side diodes) are selected. (For interpretation of the references to colour in this figure legend, the reader is referred to the web version of this article.)

Furthermore, due to enhanced signal and speed, it was also shown that this configuration might be more beneficial for dynamic TKD investigation [13] and can also be advantageous for non-conductive samples and weakly diffracting materials.

The combination of TKD and STEM imaging has been shown for both configurations. Independent of the detector configuration, STEM images can be collected from the electron transparent sample using forward scatter diodes located on the periphery of the detector screen. Fig. 1 illustrates the different configurations of the diffraction pattern detector and the imaging system coupled to it. For the off-axis TKD detector (Fig. 1(a)), only dark field images (STEM-DF) can be obtained, since the direct beam does not reach the imaging diode (shown in blue

in Fig. 1(a)). In the case of on-axis TKD (Fig. 1(b), (c) and (d)), both bright field images (STEM-BF, Fig. 1(c)) as well as dark field (STEM-DF, Fig. 1(d)) can be acquired by selecting different diodes, positioned either directly in the path of the direct beam (Fig. 1(c)) or in such a way to intercept a portion of the scattered electrons (Fig. 1(d)). It is important to emphasise at this point, that although it is common to refer to the images obtained with the middle diode in on-axis TKD (Fig. 1(c)) as STEM-BF images, they are in fact quasi-STEM-BF images. As a result of the size and proximity of the imaging diode to the sample, it is common that along with the direct beam signal, some low angle diffracted signal is also collected at the imaging diode. Consequently, the diffraction contrast of the so-called STEM-BF images obtained in this

configuration is often poor in comparison to the true STEM-BF condition. Increasing the distance between sample and detector or reducing the size of the diode are options to improve this issue. STEM images can also be obtained by selecting specific regions of interest on the phosphor screen as shown in [14–16] and by combining TKD with a solid-state STEM detector in the SEM, as shown in [17,18]. Even though there are several ways of combining the information from STEM images with TKD measurements, this combination has rarely been explored for site specific studies.

Despite the fact that the on-axis TKD configuration allows the combination of orientation mapping with high resolution BF and DF imaging, it is not possible to simultaneously obtain the two signals in an optimal manner. This is mainly due to the position of the imaging system, which requires a camera movement of approximately 20 mm from the optimal mapping position (Fig. 1(b)) to the optimal imaging position (Fig. 1(c) and (d)). This movement poses some considerable challenges for site-specific characterization of nanocrystalline microstructures and nanoparticles, due to beam and sample drift associated with such movement. In this publication, a solution to this drawback will be presented and discussed.

2. Experimental details

All data presented in this publication were obtained on a FEI Nova Nanolab 600 SEM with a Bruker e-Flash EBSD detector retrofitted with an OPTIMUS™ TKD detector head. Prior to the TKD investigation, the samples were plasma cleaned inside the microscope chamber using an Evactron decontaminator (XEI-Scientific, Redwood City, CA) for 5 min. All TKD measurements and STEM images were performed at 30 keV beam energy and with an aperture of 30 μm in high vacuum mode (apart from the in-situ investigation described below). All investigated samples were supported by a 5 nm silicon nitride membrane and positioned on the SEM microscope stage with the membrane facing the microscope pole piece and the sample facing the TKD detector [19]. No data cleaning was performed to any orientation measurement. Further details about the beam current, working distance and detector distance applied are described for each specific experiment.

2.1. Problem statement

Fig. 2 shows the images and orientation map obtained from a 30 nm Au thin film deposited on a 5 nm silicon nitride TEM window using the on-axis TKD detector. All images and orientation maps were carried out using a beam current of 1.7 nA. Fig. 2(a) and (b) were obtained in the imaging position while Fig. 2(c) and (d) in the measuring position. All images were taken with a pixel size of 2 nm, while the TKD measurement was performed with a 5 nm step size. In Fig. 2(a), the STEM-BF image collected with the middle diode of the imaging system positioned directly underneath the primary beam is shown (see also Fig. 1(c)). Fig. 2(b) shows the STEM-DF image obtained with both outer diodes (see also Fig. 1(d)). Fig. 2(c) shows the same position of the sample after the on-axis TKD detector has been moved to the measuring position. This image was acquired using all three diodes, to enhance the contrast, since a much weaker signal is arriving at the diodes when the camera is positioned optimally for diffraction pattern detection (see Fig. 1(b)). The comparison between the images shows that some of the microstructure details in the image are partially lost in the measurement position, due to the lower signal arriving at the imaging diodes. Furthermore, the camera movement can deflect the beam, leading to a shift between orientation mapping and high resolution BF/DF images (see highlighted areas and letter A on the images). Comparing the images from before detector movement with the one after, a displacement of more than 450 nm in the X direction can be measured. In cases where some microstructure features can still be recognized on the image in the measurement position, this displacement can be corrected by shifting the beam accordingly.

Fig. 3 shows the microstructure of another Au film deposited on a 20 nm silicon oxide membrane with a 0.7 nm APTMS adhesion layer. The adhesion layer controls the microstructure of the Au film and the grain size is significantly refined. In such microstructure, without features (e.g. large grains or characteristic twin boundaries), it is extremely difficult to combine a STEM image with an orientation measurement from the same position, since it is difficult to relocate the microstructure. Fig. 3(a) shows the STEM-BF and Fig. 3(b) the STEM-DF image in the imaging position, while Fig. 3(c) shows the STEM-DF image in measuring the position. All images were taken with the same resolution and pixel dwell time. The combination of an image shift in the order of few hundreds of nanometers with a low image contrast due to position of the imaging diode in relation to the sample, makes it challenging to perform site specific TKD orientation measurements on nanocrystalline materials.

The image displacement observed after detector movement is presumably related to a deflection of the beam and therefore it is related to the proximity of the detector in relation to the electron beam. Fig. 4 shows measurements of the image displacement as a function of the detector distance (or camera length) for two different beam currents: with and without a magnetic field around the sample (immersion mode). In the case of the field free mode, the larger displacement is observed in the horizontal direction (which is also the direction of the camera movement). Furthermore, the greater the detector distance is, the smaller the influence and consequently the smaller the image displacement will be. When the sample is immersed in a magnetic field, the displacement is of the same order of magnitude in both horizontal and vertical direction and decreases slightly with increasing detector distance. The influence of the beam current is much less significant. It is expected that this image displacement is microscope dependent and therefore slightly different curves might be obtained for different microscopes.

Finally, the requirement of the on-axis TKD detector movement between the two positions makes it impossible to acquire an orientation map and high-quality BF/DF images simultaneously. As previously pointed out [13], this limitation can be very critical in dynamic investigations, first because STEM images can be acquired much faster than TKD measurements, and second because in many situations the imaging-mapping combination is essential for a thorough understanding of the dynamic evolution of the microstructure.

2.2. Solution development

In the search for solutions to tackle the abovementioned issues, it was recognised that one characteristic feature of the on-axis TKD pattern is the presence of the direct beam signal at the centre of the detector screen. Fig. 5 illustrates an on-axis TKD detector in the measuring position, overlaid with a characteristic on-axis TKD pattern. Since the detector is positioned exactly below the sample, as in a TEM, the direct beam reaches the detector at the centre of the phosphor screen, saturating this area of the camera. By decreasing significantly the camera exposure time, the saturated signal can be minimized and both the direct beam signal as well as spot patterns can be recognized, however this compromises the intensity of the Kikuchi patterns. Currently the direct beam signal as well as the spot patterns are not contributing to the TKD orientation measurements. Since BF images in the SEM are produced by capturing the direct beam and electrons scattered at low angles, it would become possible to acquire them while the camera is in the measuring position by placing an imaging diode at the centre of the screen exactly where this signal is arriving. In the following section, a prototype detector including this additional centre diode will be described and the results comparing it to the commercially available on-axis TKD detector will be presented.

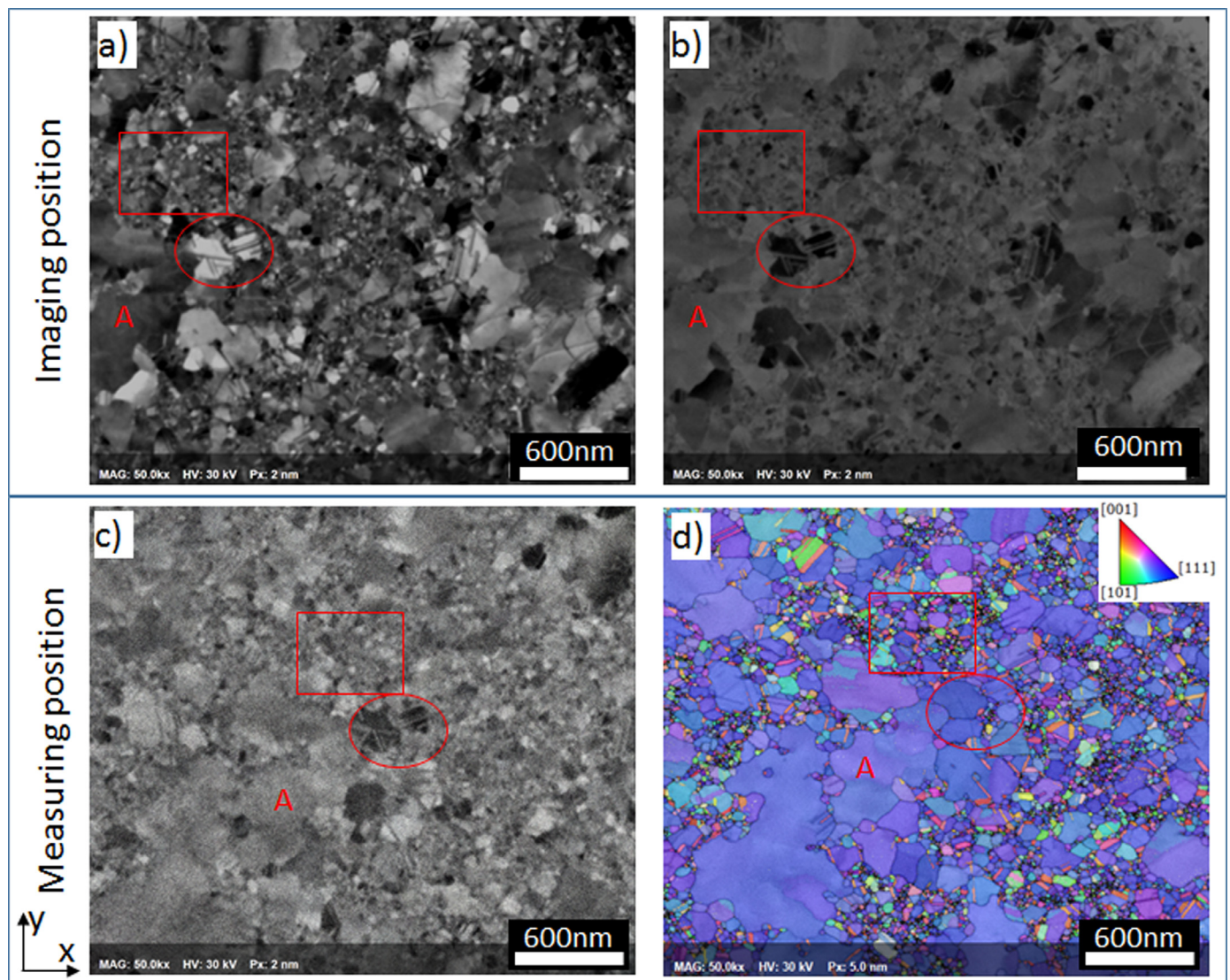


Fig. 2. (a) STEM-BF image and (b) STEM-DF image obtained in the imaging position. (c) STEM-DF image obtained in the measuring position and corresponding orientation measurement (d), where an inverse pole figure map of the film growth direction is overlaid with the pattern quality map. Red highlighted areas and the letter A indicate the same position in all four images. (For interpretation of the references to colour in this figure legend, the reader is referred to the web version of this article.)

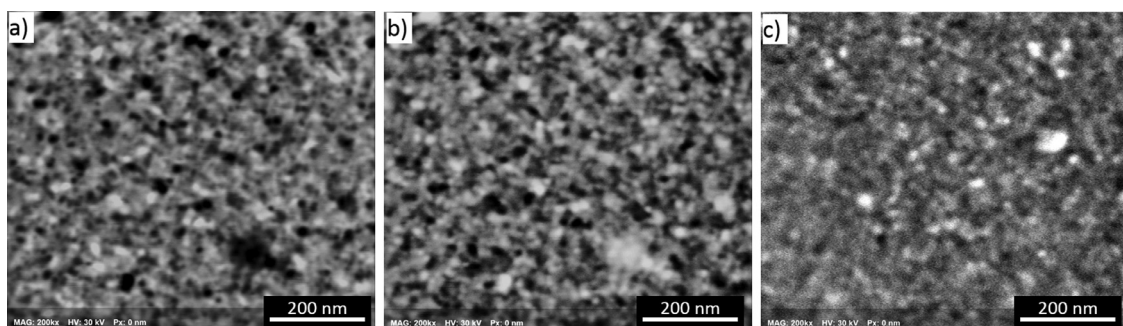


Fig. 3. STEM images of a nanocrystalline Au film acquired with the imaging diode. (a) is a STEM-BF image and (b) STEM-DF image both acquired with the detector in imaging position. And (c) is a STEM-DF image acquired with the detector in measuring position.

3. Results and discussion

3.1. Building of the prototype

Adding a silicon diode at the centre of the phosphor screen to

achieve simultaneous on-axis TKD measurements and BF-STEM imaging required the modification of the Bruker OPTIMUS detector. To this end, a customized scintillator screen has been manufactured with a hole of 4 mm diameter at its centre. The standard imaging diode of an OPTIMUS detector was modified to fit the hole in the screen. Fig. 6(a)

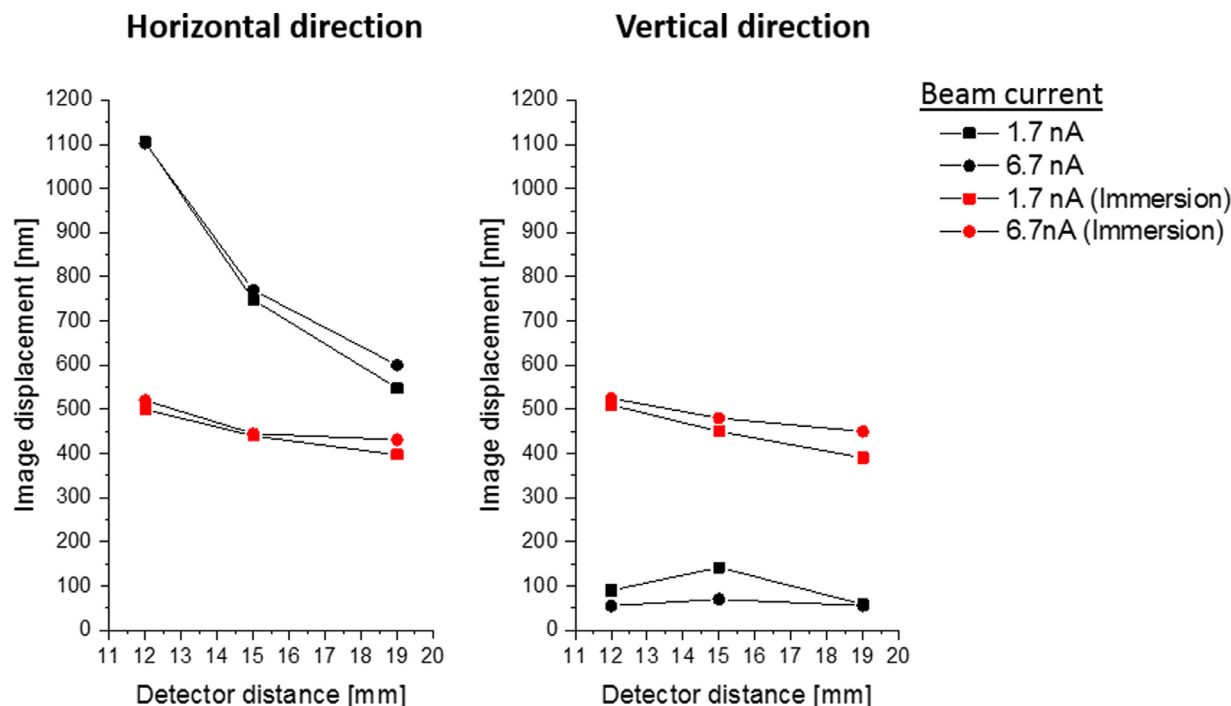


Fig. 4. Measurement of image displacement in horizontal and vertical direction when moving the TKD detector from the imaging position to the measuring position at different currents and detector distances with and without immersion mode (sample immersed in magnetic field).

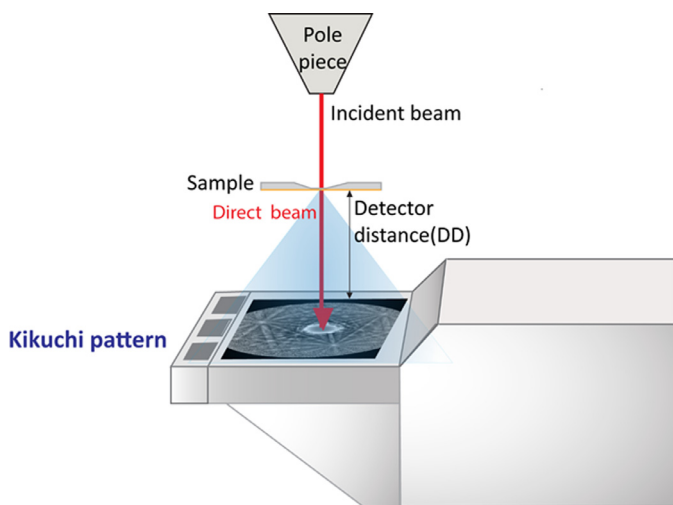


Fig. 5. Schematic representation of the on-axis TKD detector in the measuring position with an overlaid TKD pattern, showing the oversaturated signal at the centre of the TKD pattern. (For interpretation of the references to colour in this figure legend, the reader is referred to the web version of this article.)

shows the in-house built prototype, and Fig. 6(b) illustrates the schematic of the screen backside. Since the silicon diode was slightly smaller than the hole in the screen, a piece of silicon wafer was used to fix it to the backside of the scintillator screen (Silicon Bridge in Fig. 6). The electrical connection of the extra diode was achieved in two steps: first, a thick Au film was deposited, with help of a mask, around the hole and on the far edge of the screen, followed by a second thinner Au film deposited on the back of the entire screen. The Au film was scratched in two places (as illustrated in Fig. 6(b)), to enable using the two halves as a means of conducting the signal towards the edge of the screen, thus avoiding using wires in the optical path of the detector. Two thin Au wires were then soldered to connect the diode to the thick Au-coating surrounding the hole and two wires were used to connect the Au film halves to the detector cables. The cables were then connected to the

plugs already available for the middle diode of the standard OPTIMUS TKD detector. The new modified screen was then placed on the OPTIMUS TKD detector (Fig. 6(a)).

It is important to point out that this is an in-house built prototype, which adapted the existing detector head to demonstrate the concept behind the new setup. For this reason, the centre diode had to be linked to one of the existing connections of the imaging system. Therefore, in this prototype the standard middle diode (shown in red in Fig. 1(c)) is inactive and cannot be used for STEM-BF images in the imaging position. Thus, a comparison between STEM-BF images acquired with the new centre diode and the original middle diode was not possible.

3.2. Testing the prototype

Fig. 7 shows images and orientation maps acquired from a 30 nm Au thin film using the prototype described above. All images were obtained with the TKD detector in the measuring position and a beam current of 0.32 nA without detector movement. Fig. 7(a) shows the STEM-DF images obtained with the two diodes located outside the detector screen, as highlighted in red in Fig. 7(b). Fig. 7(c) shows the STEM-BF image collected with the new central diode at the same sample position. An inverse pole figure (IPF) map overlaid with the pattern quality map of the blue highlighted area is shown in Fig. 7(d) and 7(e); Fig. 7(d) shows grain orientation in the film growth direction and Fig. 7(e) the in-plane orientation. The TKD measurement was collected with a step size of 3 nm, while the images have a pixel size of 1 nm.

Avoiding detector movements would be advantageous, even in samples where microstructure or sample features allow easy identification after the image shifts due to detector relocation. Moreover, particularly advantageous in cases where those easily recognizable features are not present in the microstructure. It is also important to emphasise that since the major diffraction signal investigated in TKD derives from the sample exit surface [19], in most cases, the area of interest is positioned away from the microscope pole piece, and consequently away from the secondary electron detector. Consequently, often the secondary electron image does not facilitate the location of the site and STEM images must be used. Furthermore, due to the higher

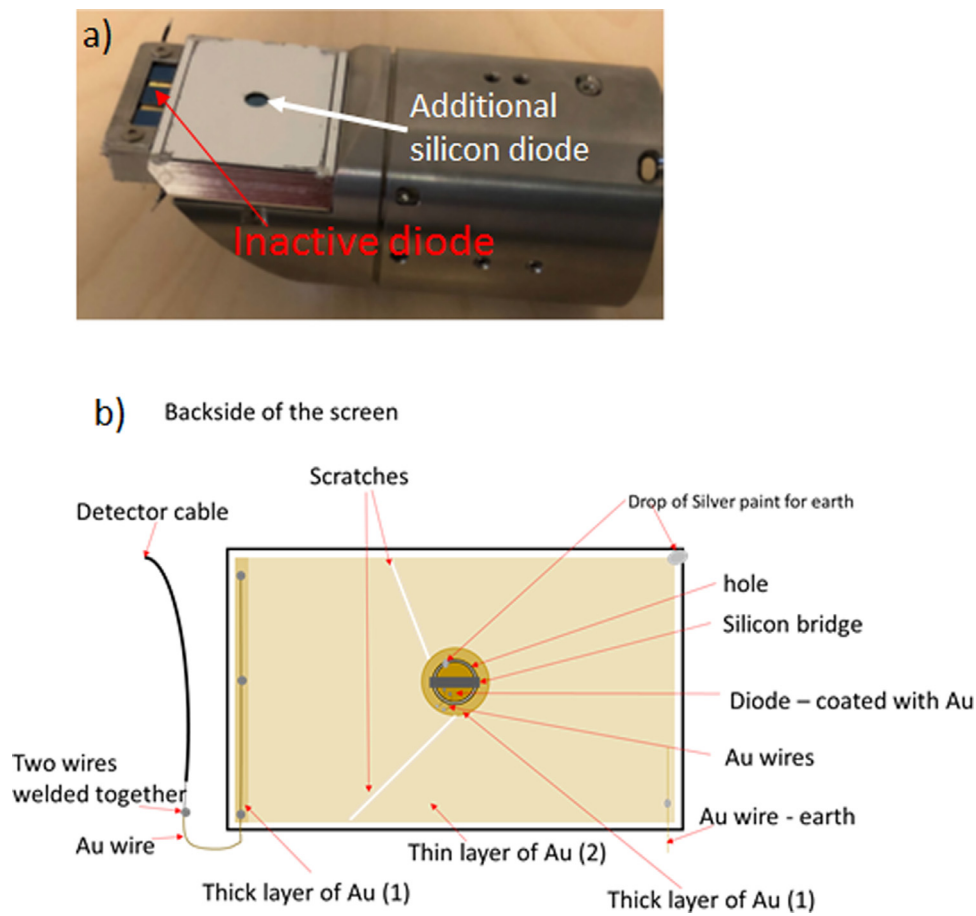


Fig. 6. Image (a) and schematic representation (b) of the in-house built prototype with an imaging diode located at the centre of the phosphor screen. (For interpretation of the references to colour in this figure legend, the reader is referred to the web version of this article.)

resolution achieved in STEM images in comparison with TKD orientation measurements, the combination of both images of the same position allows better understanding of the microstructure.

Nevertheless, there are still remaining challenges: e.g., the

compromise of finding the best microscope setup that enables both high quality STEM imaging and the required quality of the TKD measurement. The imaging diode used in this work was exactly the same of that of the conventional on-axis TKD detector and it becomes saturated with

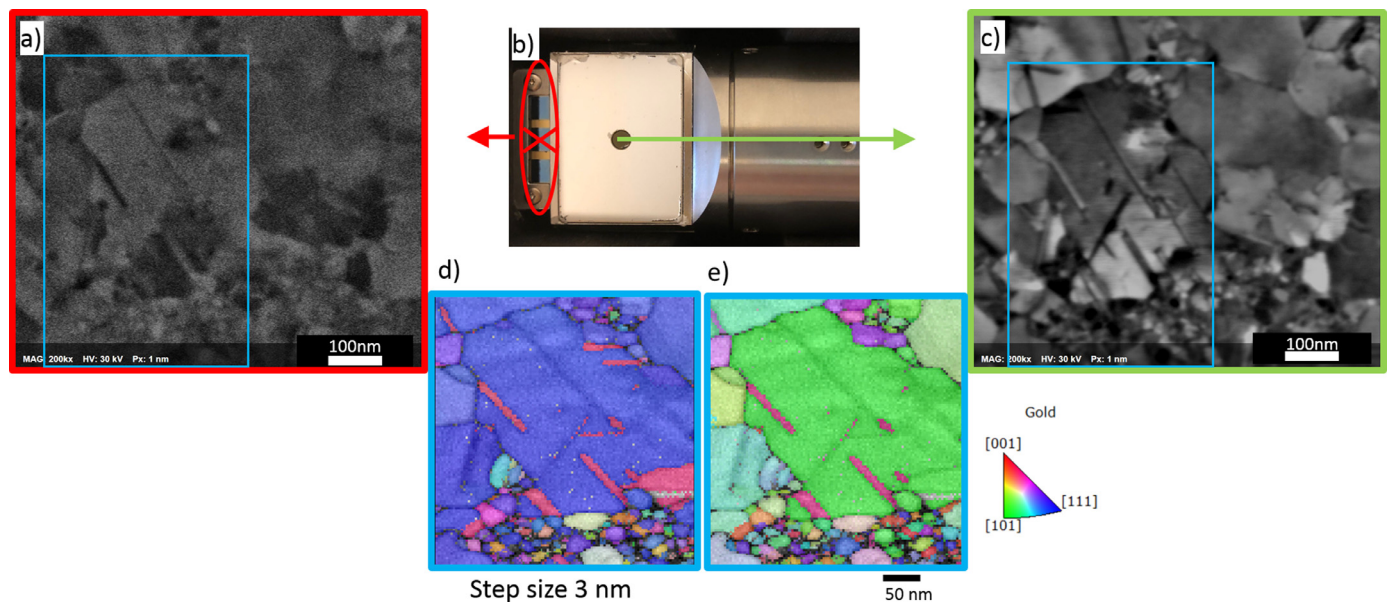


Fig. 7. STEM images and TKD measurements obtained with the prototype detector in the measuring position. (a) STEM-DF image; (b) Prototype detector indicating which diodes are used for each image; (c) STEM-BF image; inverse pole figure overlaid with the pattern quality map of (d) the out of plane direction and (e) the in plane direction respectively. (For interpretation of the references to colour in this figure legend, the reader is referred to the web version of this article.)

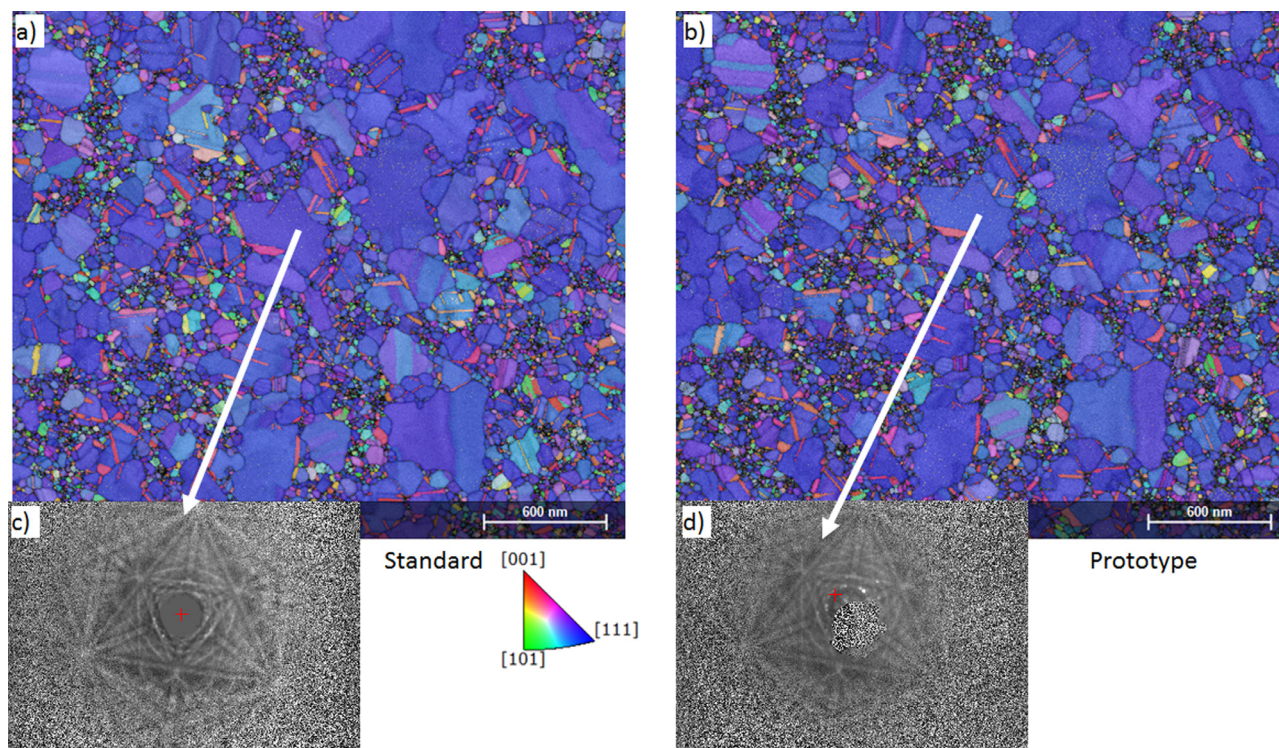


Fig. 8. Comparison of a TKD measurement carried out on the same position of the sample with the (a) standard on-axis TKD detector and (b) with the prototype detector. Comparison of a TKD pattern from the same position obtained with the (c) standard on-axis detector and (d) with the prototype detector. The red cross in (c) and (d) represents the pattern centre. Both measurements were taken with the same microscope and measurement parameters and in both cases, a static background was subtracted from the raw TKD pattern. (For interpretation of the references to colour in this figure legend, the reader is referred to the web version of this article.)

too much signal (high beam current), resulting in poor images. The best STEM image resolution is often achieved at lower beam currents than TKD measurements require. In the example showed in Fig. 7, a relatively low beam current was chosen, improving the quality of the STEM image, but requiring relatively long TKD measurement time. In a well-aligned microscope, changing the beam current between imaging and mapping is not associated with experimental difficulties, however it can in some cases require microscope realignment.

3.3. Comparison to standard detector

An expected question at this point would be to ask how the TKD measurements carried out with this prototype compare with those produced with the commercially available on-axis detector. Fig. 8 shows two orientation maps obtained from the same sample position (sample: 30 nm Au film supported on a 5 nm silicon nitride membrane). Fig. 8(a) shows the map collected with the standard on-axis TKD detector and Fig. 8(b) with the new prototype configuration. Both measurements were carried out using the same parameters: 30 kV accelerating voltage, 1.7 nA beam current, 30 μ m aperture, 5 mm working distance, 13.6 mm detector distance at high vacuum and with a pattern resolution of 320 \times 240 pixels, 10 ms exposure time and 5 nm step size. The measurement with the prototype was performed prior to the one with the standard detector. The microscope stage was fixed while the detector head was exchanged, and the sample was plasma cleaned for 5 min inside the microscope chamber between the two maps. No data post-processing was applied to any of the maps.

The comparison between the two orientation maps in Fig. 8(a) and (b) reveals a slight misorientation of the two maps. This can also be observed on the Kikuchi patterns shown in Fig. 8(c) and (d), as the pattern centre of the prototype (indicated by the red cross) is offset. This is a consequence of a small misalignment of the prototype detector head in the x direction. From the pole figure plots and from

measurements of misorientation between the same grains in both maps, it is deduced that the measurements are about 5° off from each other.

Further comparison reveals that both the indexing rate and the pattern quality of the prototype are slightly reduced. In total 92.2% of the data was indexed for the standard detector and 88.4% for the prototype, in both cases considering at least 5 detected bands and a band mismatch (BMM) angle of maximum 1.8°. Moreover, the two patterns in Fig. 8(c) and (d) show a noticeable reduction of the intensity, especially at large angles. This contributes to the reduction of the pattern quality metric and indexing rate, and is most probably a consequence of the presence of the Au film on the back of the screen (Fig. 6(c)), which filters some of the photons/light produced by the screen, thereby decreasing the intensity of the patterns. Although both quality values reveal a disadvantage of the prototype detector, the results provide valuable details that will help in the design of the final solution.

Fig. 9 illustrates the comparison between the two measurements. In all graphs, the prototype data is plotted in black while the standard detector is plotted in red. In Fig. 9(a) the pattern quality is compared: it is possible to observe that the curve is shifted to lower pattern quality for the prototype. It is highly likely that optimizing the thickness of the Au film on the back of the camera or an improved detector design would improve the pattern quality and make it more comparable with that achieved with the standard on-axis detector. In Fig. 9(b) a comparison of the indexing rate as a function of the minimum number of detected bands fitting the solution is shown. This graphic representation was made by a stepwise increase of the minimum number of detected bands required for a successful indexing of the pattern. Independently from the number of bands considered, the standard detector always reveals a slightly better indexing rate. Here again an improvement of the pattern quality for the prototype might be a solution to this small difference. Nevertheless, when comparing the orientation precision of both detectors, the prototype seems to bring

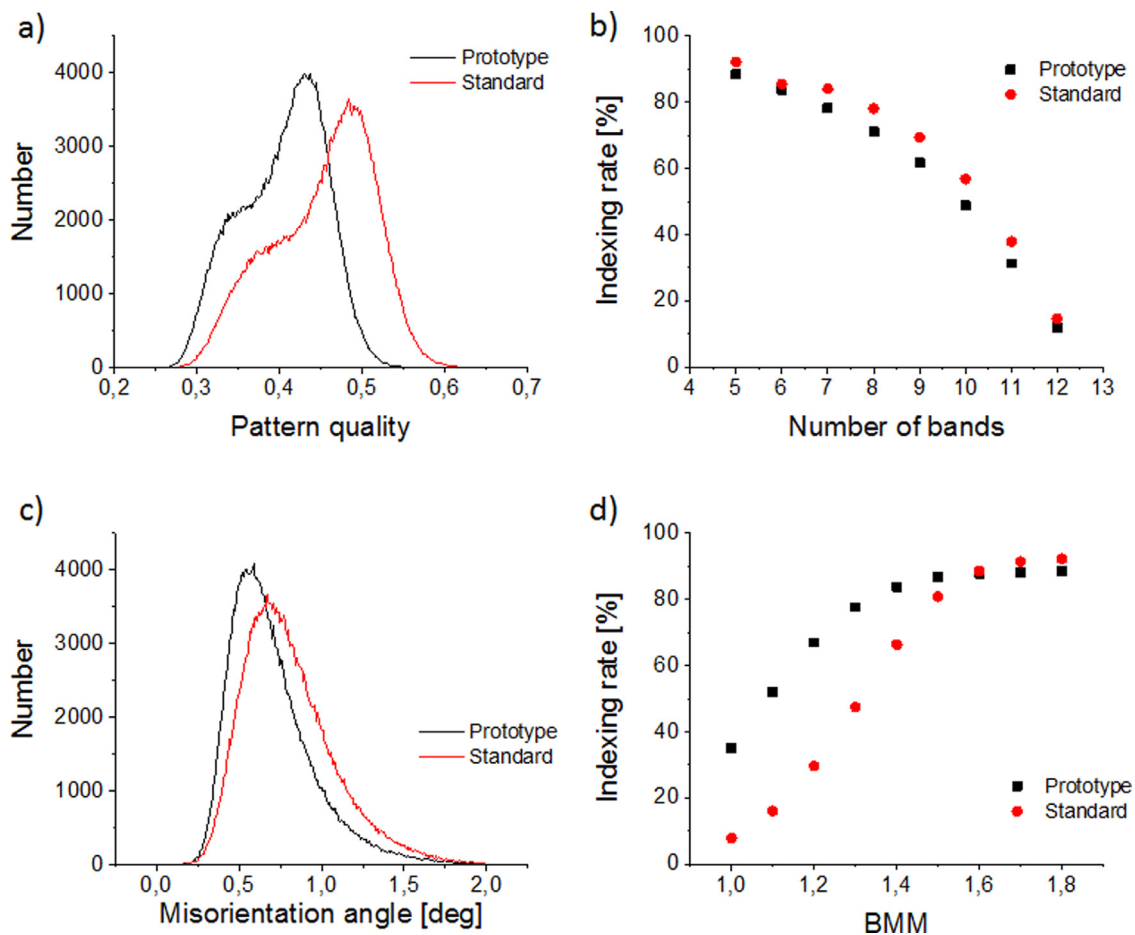


Fig. 9. Comparison between prototype (Black) and standard detector (Red) of: a) pattern quality histogram; b) indexing rate as a function of the minimum number of detected bands; c) kernel average misorientation (KAM) for a maximum of 2° deviation; d) indexing rate as a function of the maximum band mismatch angle (BMM). (For interpretation of the references to colour in this figure legend, the reader is referred to the web version of this article.)

improvements to band detection. The kernel average misorientation (KAM) is one of the parameters that can be used to measure the orientation precision [20] in non-deformed samples. In Fig. 9(c) a histogram of KAM values for both detectors is plotted considering a kernel of 3×3 data points at a step size of 5 nm and a maximum of 2° deviation. Although the shift of the curve is very small, it is possible to observe a decrease in the degree of local misorientation for the prototype in comparison to the standard detector. To verify this finding, another estimation of the indexing precision is presented in Fig. 9(d). In this case, both maps are compared in terms of indexing rate as a function of the maximum band mismatch angle (BMM). The BMM is defined as the maximum angle that the measured band position can deviate from the calculated position of the band. A BMM in the range of 1.6° to 1.8° is considered adequate as it provides the best compromise between highest indexing rate and lowest rate of mis-indexed points. However, the lower the BMM, the more precise the orientation determination is, i.e. lower orientation noise. This plot reveals that in the “upper” range of BMM values, the standard detector performs to a small extent better than the prototype. However, by decreasing the allowed BMM values below 1.6° into ranges of lower orientation noise results, there is an inversion of this trend and the indexing rate of the prototype is considerably better. The lower orientation noise explains the higher indexing rates at conservative BMM values seen in Fig. 9(d). On the other hand, the prototype produces less intense patterns/bands and therefore it is likely that the software will detect fewer bands on these patterns as compared with the patterns acquired with the standard on-axis detector. The lower number of detected bands is probably the main cause for the inversion trend seen in the graph in Fig. 9(d). In other words, the

prototype on-axis detector produces patterns with fewer visible bands, which leads to lower probability for successful indexing thus producing lower indexing rates. This is also consistent with the results in Fig. 9(b) where the spread between the two curves increases after a minimum of 7 bands is used for indexing.

Although there is still room for improvement of the design of the prototype, the experimental results demonstrate the proof of principle and the advantages of having an additional detector at the centre of the screen.

Establishing an electrical connection between the diode located at the centre of the screen and the existing connection is one of the challenges of this solution. Wires along the optical path may be detected as bands by the indexing routine and compromise the indexing performance of the system. Using a continuous metallic layer (as chosen in this prototype), also on the optical path of the detector, prevents wires being mistakenly indexed as Kikuchi bands but reduces the signal arriving to the camera. Adjusting beam current and/or camera exposure time might be enough to compensate for the reduced signal without compromising the indexing performance. Reducing the thickness of the metallic film and experimenting with other conductive layers are possible improvements that could be investigated in the future. A further alternative would be to add the imaging diode to the mirror (which is located below the detector screen with an angle of 45° to the camera) [2] instead of adding it to the hole in the phosphor screen and connecting the diode behind the mirror, keeping the connections out of the light path of the camera. Another possibility which could be investigated in the future is to use the silicon diode both as an imaging system as well as a mirror.

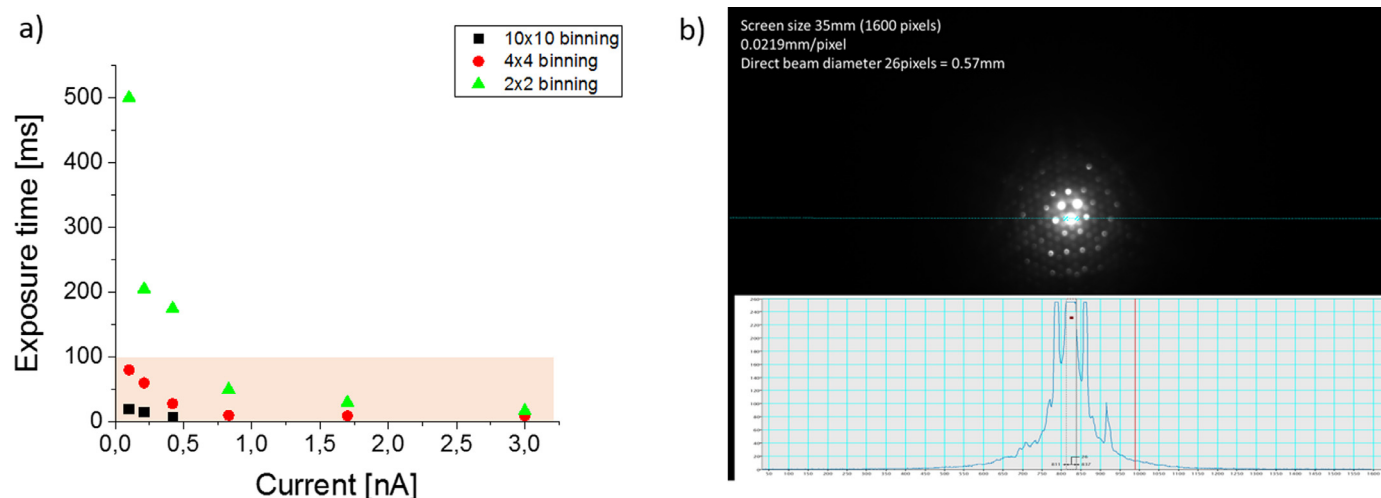


Fig. 10. (a) Correlation between current, exposure time and pattern resolution required for obtaining measurable TKD patterns when using a centre diode of 4 mm diameter to obtain TKD measurements from a 15 nm thin Au film. The red shaded area represents acceptable measurement parameters. (b) Measurement of the direct beam diameter from high resolution (1600×1200) spot pattern of a 15 nm Au film acquired with a TKD detector distance of 14.8 mm and exposure time of 28.1 ms. (For interpretation of the references to colour in this figure legend, the reader is referred to the web version of this article.)

However, some limitations are clearly imposed by adding the imaging system to the centre of the phosphor screen. The diameter of the overexposed area of the phosphor screen depends on microscope parameters, material, sample thickness and on measurement parameters. A perfect diode size is therefore very difficult to estimate. The current design, with a centre diode of 4 mm, was arrived at after considering “standard measurement parameters”, which means reasonable speed at standard beam current. This size was estimated by investigating the range of beam currents, exposure times and pattern resolutions over which the existing diode would be suitable for not only blocking the saturated signal but also allowing enough diffraction signal to be available for orientation mapping. For this estimation the material, sample thickness, detector distance and beam aperture were kept constant. Fig. 10 shows plots of the exposure time variation as a function of the beam current for various pattern resolutions. This graph shows, for example, that for measuring on a 15 nm Au film with an aperture of $30 \mu\text{m}$ at 16 mm detector distance with a 800×600 pixels pattern and 0.1 nA current, an exposure time of 500 ms would be required for obtaining enough signal for an orientation map. However, using a beam current of almost 1 nA, the exposure time would be reduced by a factor of 10 and a reasonable speed would be achieved for mapping (50 ms). Furthermore, it shows that very fast maps with very low-resolution patterns, e.g. 160×120 pixels, would only be possible at very low beam currents, otherwise a too large area of the detector would be overexposed (this is also the case for the standard detector). The red shaded area in Fig. 10 shows the range of parameters that would be considered standard during orientation mapping.

The current diode size was also estimated based on the standard setting for TKD measurements, in which the overexposed area is, in general, set to 1/10 of the size of the phosphor screen to achieve best contrast conditions also at high scattering angles. Increasing or decreasing the size of the centre diode is an option that will be evaluated in the future. Potentially, multiple screens could be designed with varying diode sizes for different experimental conditions, which could be exchanged easily by simply replacing the detector screen.

Furthermore, as mentioned above, the image diode also becomes saturated, making it impossible to acquire good quality BF-STEM images at high beam current, very small thickness or when imaging nanoparticles suspended on thin amorphous membranes. These factors also limit the possibility of combining TKD measurements and STEM images with the prototype detector at high beam currents.

As previously mentioned, the BF-STEM images obtained with both

the standard on-axis TKD detector as well as with the prototype cannot be considered true BF-images due to the size and distance of the detector to the sample. In general, the diode is too large to allow the collection of only the direct beam thus enabling the true bright field contrast. Fig. 10(b) shows a high resolution (1600×1200) pixels TKD pattern of a 15 nm Au thin film with very low exposure time (28 ms) at a detector distance of 14.8 mm. From this image the size of the direct beam can be estimated to be in the order of 0.57 mm. It is however also evident, that although the detector saturation is reduced, it still presents, therefore it can be concluded that the size of the beam is even smaller. With this result in mind, an interesting direction for further development is to use a segmented imaging diode (annular or quadrant), similar to commercial available solid state STEM detectors [21]. With this, true bright field images can be acquired and different segments could be selected for BF- and DF-STEM images and depending on the sample thickness. As it can be observed in Fig. 10(b), the signal behind the saturated area of the camera contains useful information. This information is currently unexplored in TKD, fundamentally for two reasons: first, the TKD automated indexing software is designed to index Kikuchi bands and not spot patterns. Second, to increase the quality of the Kikuchi patterns and consequently the indexing rate of the software, it is important to obtain a good intensity across the phosphor screen and to obtain this, the central area of the camera becomes saturated (see Fig. 11). Fig. 11 shows the difference in the Kikuchi band contrast and the size of the saturated area on the centre of the screen by increasing the beam current from 1.7 nA to 6.7 nA. All patterns in Fig. 11 were acquired with resolution of 1600×1200 pixels and with an exposure time of 28 ms (Fig. 11(a) is the same as Fig. 10(b)).

Although spot patterns are not yet been used for automatic indexing of TKD orientation measurements, it is expected that future development will enable this possibility. Spot patterns, in contrast to Kikuchi patterns, are observed even at very low thickness, when incoherent scattering is not sufficient, and contain information of overlapping crystals. Additionally, Kikuchi patterns become blurred in heavily deformed material, complicating the indexing [12,22]. Therefore, it would certainly be useful to combine indexing of spot and Kikuchi patterns on samples with varying thickness (or very thin samples), varying composition and on highly deformed materials. Developing a filter, which allows combining both signals with high efficiency is part of our current ongoing development and will be described and discussed in a future publication. Although the prototype detector presented in this work is located exactly in the area in which this signal is

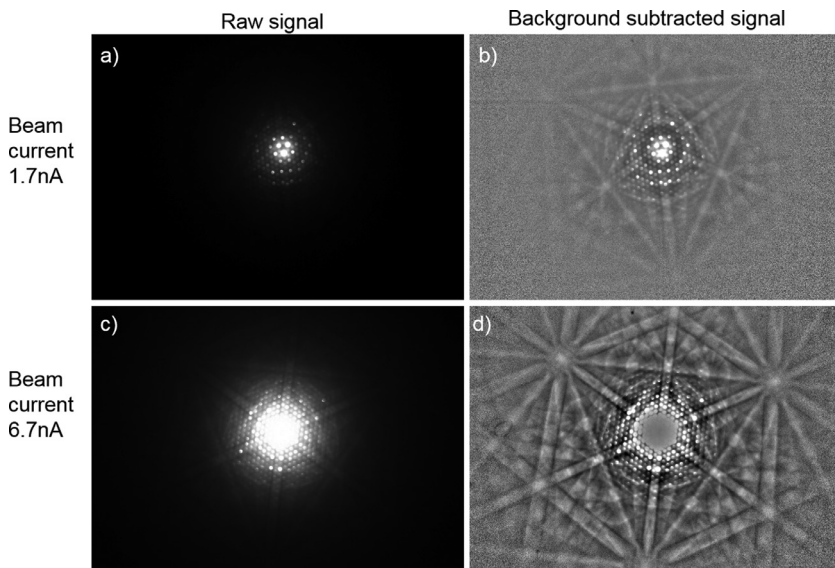


Fig. 11. Raw and background processed signals obtained on the on-axis TKD detector for a 15 nm Au film deposited on a 5 nm Si_3N_4 membrane. Patterns obtained at 30 kV and detector distance of 14.8 mm with a resolution of 1600×1200 pixels. (a) and (b) were obtained at a beam current of 1.7 nA, while (c) and (d) were obtained at 6.7 nA. (a) and (c) are the raw pattern signal, while in (b) and (d) the background signal was subtracted to enhance the Kikuchi pattern contrast.

arriving at the detector, and therefore covers this information, it can be foreseen that in the future TKD detectors will have different phosphor screens for different application goals.

3.4. Dynamic experiments with the prototype

A final result, which in fact illustrates the significant advantages of combining STEM-BF images with TKD orientation measurements without detector movement, is the ability of combining these two signals in time-resolved experiments. The combination of TKD measurements with in-situ heating of thin films using MEMS-based heating holders has been demonstrated recently [13]. However, extending this combination with in-situ STEM-BF images permits an even better time resolved microstructure investigation and adds significant information to the understanding of material behaviour. Such experiments are not restricted to thin films, and can be extended to nanoparticles and even electron transparent lamellas produced by focused ion beam [23].

To demonstrate the capability of the prototype for dynamic studies, a 20 nm Au thin film was deposited on a DENS Solution MEMS-based heating chip and investigated during heating cycles of 30 min at 150 °C, 200 °C and 250 °C. The sample was examined using an accelerating voltage of 30 kV, beam current of 1.7 nA, with a 30 μm aperture, at a working distance of 5 mm and detector distance of 14 mm at low vacuum condition (50 Pa water pressure). The patterns were acquired with an exposure time of 22 ms and at resolution of 320×240 pixels. Furthermore, a step size of 3 nm was chosen for the TKD measurements and an image pixel size of 0.5 nm for the STEM-BF images. STEM-BF images were acquired at the respective elevated temperatures and saved manually at approximately every 45 s (time required to scan the image and save it manually). After every heating cycle the sample was cooled down to room temperature for the TKD measurements, which were typically completed after approximately 40 min for each one. It is important to point out here that, although the STEM images and the TKD measurements were acquired without any detector movement and within the same software, they were not acquired simultaneously, due to current restrictions of the software.

Furthermore, even though no detector or sample movement was required during the experiments, thermodynamic drift of the sample was clearly observed during the heating stage. No drift correction was performed during the heating cycles of 30 min; however, beam shift was applied to relocate the area of interest in the measurement field for conducting the TKD measurements at the same position after every temperature cycle.

Fig. 12 shows a series of STEM-BF images and inverse pole figure

maps (out of plane) obtained from the 20 nm Au film during the heating experiment. These maps were processed to remove a small amount of zero solution data points (less than 1% of the data) and are represented with high angle grain boundaries in black, low angle in white and twin boundaries in red. A video display of all STEM-BF images obtained at elevated temperature is shown in the supplementary material. The video as well as the TKD measurement shows clearly the grain growth and the microstructure change with the temperature. Since TKD gives quantitative data from the microstructure, it is evident that TKD provides much more information on the microstructure, grain boundaries and texture evolution of the film than the STEM images. For example, from the TKD data it can be extracted that the average grain size increases from 75 to 200 nm during the experiment and that after the experiments more than 90% of remaining grains are orientated with $[111]//\text{growth direction}$. Nevertheless, the STEM-BF images provide details that are not spatially resolved by the TKD measurement, e.g. the defect inside the highlighted grains in Fig. 12. The formation and dynamic behaviour of those defects can be followed on the video presented in the supplementary material. Furthermore, STEM images are acquired much faster than orientation maps, and consequently provide a much more realistic picture of the microstructure evolution during the heating process. This realistic picture combined with the quantitative data obtained by TKD allows detailed understanding of the dynamic process and improves the capabilities of the technique. Such a combination is more powerful than previously explored characterization studies via orientation mapping (TKD) and observing the evolution by imaging before and after in-situ heating [24].

It is however important to notice that STEM images and TKD orientation mapping are complementary techniques. Data obtained from multi-layered samples have shown that each signal originates from a different depth in the sample, meaning that in some cases the STEM images and TKD data are not necessarily identical. This effect is currently under more detailed investigation and will therefore be presented and discussed in a future publication.

4. Summary and conclusions

In this work, we presented a modification of the commercially available on-axis TKD detector to enable a more accurate and easier combination of orientation measurements with STEM-BF images for the investigation of electron transparent samples. The detector presented here removes the requirement of a detector movement between two different positions for acquisition of STEM-BF images and TKD measurements, making site specific and simultaneous imaging and

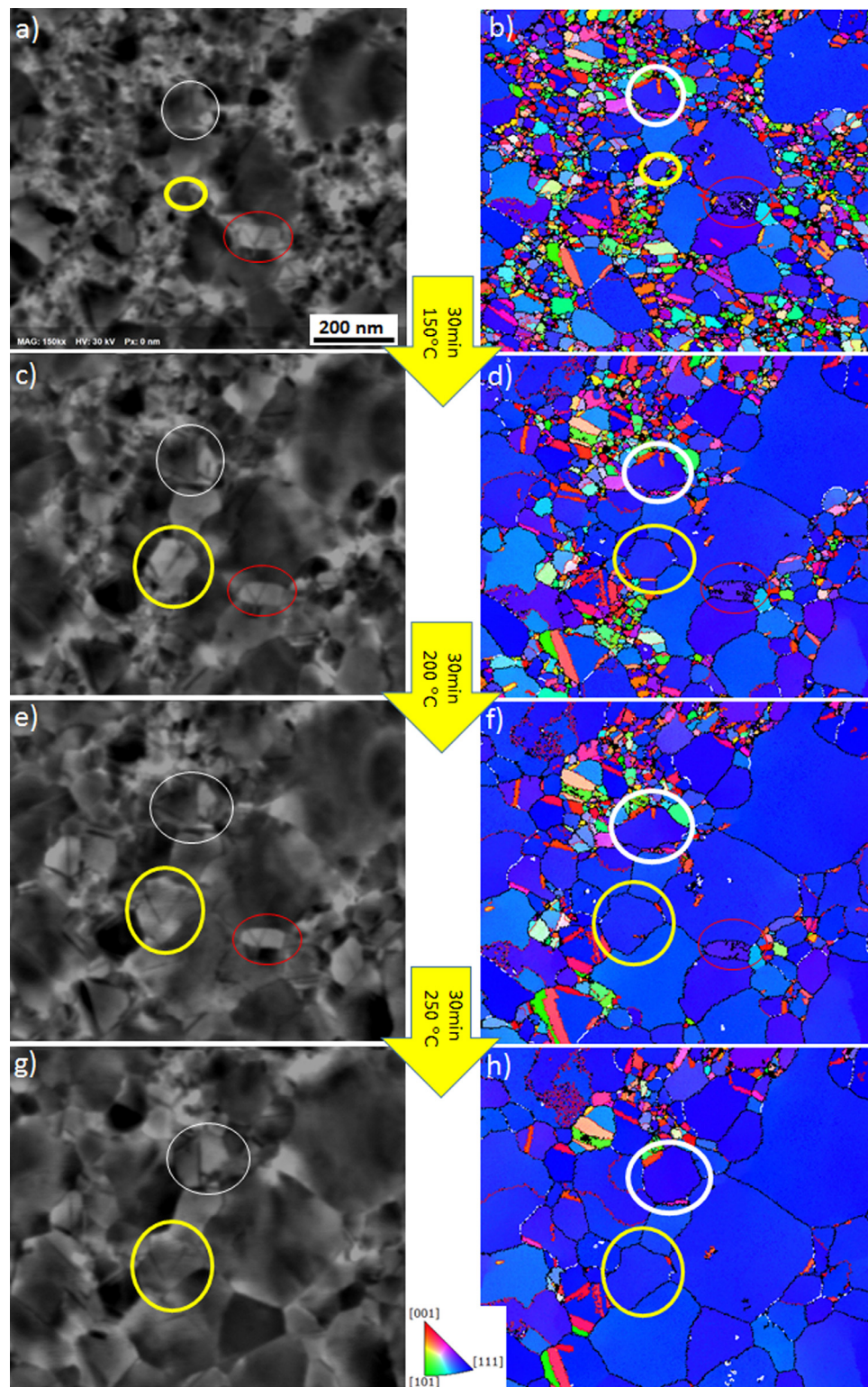


Fig. 12. Microstructure evolution with temperature. (a), (c), (e) and (g) STEM-BF images obtained with the new imaging diode. (b), (d), (f) and (h) TKD inverse pole figure map of the film growth direction. (a) and (b) were acquired at room temperature; (c) and (d) after heating for 30 min at 150 °C; (e) and (f) after heating for 30 min at 200 °C; (g) and (h) after heating for 30 min at 250 °C. All images and maps acquired with the prototype detector from a 20 nm Au film deposited on a silicon nitride membrane at 30 kV and 1.7 nA.

orientation mapping at the same site significantly easier. The newly developed prototype features a diode at the centre of the TKD screen. This additional imaging system does not significantly compromise or impose difficulties for the use of an on-axis TKD detector, since the additional diode is located in the area of the detector which was not

previously utilised, due to the saturated signal arriving at this region by the direct transmitted electrons reaching the phosphor screen.

The performance of the prototype was compared to the standard on-axis detector and showed great promise. Although a slight decrease in pattern quality was observed for the new prototype detector, this issue

will most probably be overcome by optimising the detector design and construction. The results revealed that despite the decrease in pattern contrast, the indexing precision is as good as or even better than the standard detector. The range of measurement parameters in which the advantage of this new detector is applicable is currently limited. Variations of this idea are clearly possible, as for example by adapting the size of the diode and/or using an annular segmented diode.

The most promising advantage of the new detector is the combination of TKD with STEM-BF images for time-resolved experiments, which will, hopefully, soon be applied to investigate not only dynamic heating, but also deformation and reactions of electron transparent samples in the SEM.

It is evident that the detector presented in this work represents a step forward in improving the capabilities of the TKD technique to characterize nanocrystalline materials in the SEM. There are however a range of parameters that require improvements to make this solution widely applicable: these include optimizing the connection of the centre diode without compromising the quality of the Kikuchi pattern, developing the software to enable automated and hopefully also simultaneous acquisition of STEM images and TKD measurements and taking into consideration a change of the imaging system to enable acquisition of high quality BF-STEM images in this set up.

Acknowledgements

The author would like to thank Marco Beleggia, DTU Nanolab, for his comments to the manuscript. Bruker Nano GmbH (BNA) is gratefully acknowledged for the loan of the OPTIMUSTM TKD detector head and for the support for making the prototype. This work was supported by DTU Nanolab. The prototype was built and all investigations were carried out at the Technical University of Denmark at DTU Nanolab (former DTU Centre for Electron Nanoscopy).

Funding

This research did not receive any specific grant from funding agencies in the public, commercial, or not-for-profit sectors.

Supplementary materials

Supplementary material associated with this article can be found, in the online version, at [doi:10.1016/j.ultramic.2019.112812](https://doi.org/10.1016/j.ultramic.2019.112812).

References

- [1] R.R. Keller, R.H. Geiss, Transmission EBSD from 10 nm domains in a scanning electron microscope, *J. Microsc.* 245 (2012) 245–251, <https://doi.org/10.1111/j.1365-2818.2011.03566.x>.
- [2] J.J. Fundenberger, E. Bouzy, D. Goran, J. Guyon, H. Yuan, A. Morawiec, Orientation mapping by transmission-SEM with an on-axis detector, *Ultramicroscopy* 161 (2016) 17–22, <https://doi.org/10.1016/j.ultramic.2015.11.002>.
- [3] B.N. GmbH, QUANTAX EBSD with OPTIMUS™ TKD – Transmission Kikuchi Diffraction Under Optimum Conditions, (2015).
- [4] H. Yuan, E. Brodu, C. Chen, E. Bouzy, J.-J. Fundenberger, L.S. Toth, On-axis versus off-axis transmission Kikuchi diffraction technique: application to the characterisation of severe plastic deformation-induced ultrafine-grained microstructures, *J. Microsc.* 0 (2017) 1–11, <https://doi.org/10.1111/jmi.12548>.
- [5] F. Niessen, A. Burrows, A.B. da S. Fanta, A systematic comparison of on-axis and off-axis transmission Kikuchi diffraction, *Ultramicroscopy* 186 (2018) 158–170, <https://doi.org/10.1016/j.ultramic.2017.12.017>.
- [6] A. La Fontaine, H.-W. Yen, P. Trimby, S. Moody, S. Miller, M. Chensee, S. Ringer, J. Cairney, Martensitic transformation in an intergranular corrosion area of austenitic stainless steel during thermal cycling, *Corros. Sci.* 85 (2014) 1–6, <https://doi.org/10.1016/j.corsci.2014.04.048>.
- [7] J. Hu, A. Garner, N. Ni, A. Gholinia, R.J. Nicholls, S. Lozano-Perez, P. Frankel, M. Preuss, C.R.M. Grovenor, Identifying suboxide grains at the metal–oxide interface of a corroded Zr–1.0%Nb alloy using (S)TEM, transmission-EBSD and EELS, *Micron* 69 (2015) 35–42, <https://doi.org/10.1016/j.micron.2014.10.004>.
- [8] M. Abbasi, M. Dehghani, H.-U. Guim, D.-I. Kim, Investigation of Fe-rich fragments in aluminum-steel friction stir welds via simultaneous transmission Kikuchi diffraction and EDS, *Acta Mater* 117 (2016) 262–269, <https://doi.org/10.1016/j.actamat.2016.06.064>.
- [9] M. Abbasi, D.-I. Kim, H.-U. Guim, M. Hosseini, H. Danesh-Manesh, M. Abbasi, Application of transmitted Kikuchi diffraction in studying nano-oxide and ultrafine metallic grains, *ACS Nano* 9 (2015) 10991–11002, <https://doi.org/10.1021/acsnano.5b04296>.
- [10] N. Brodusch, H. Demers, R. Gauvin, Nanometres-resolution Kikuchi patterns from materials science specimens with transmission electron forward scatter diffraction in the scanning electron microscope, *J. Microsc.* 250 (2013) 1–14, <https://doi.org/10.1111/jmi.12007>.
- [11] E. Brodu, E. Bouzy, Depth resolution dependence on sample thickness and incident energy in on-axis transmission Kikuchi diffraction in scanning electron microscope (SEM), *Microsc. Microanal.* 23 (2017) 1096–1106, <https://doi.org/10.1017/S1431927617012697>.
- [12] E. Brodu, E. Bouzy, J.-J. Fundenberger, Diffraction contrast dependence on sample thickness and incident energy in on-axis transmission Kikuchi diffraction in SEM, *Ultramicroscopy* 181 (2017) 123–133, <https://doi.org/10.1016/j.ultramic.2017.04.017>.
- [13] A.B. Fanta, M. Todeschini, A. Burrows, H. Jansen, C.D. Damsgaard, H. Alimadadi, J.B. Wagner, Elevated temperature transmission Kikuchi diffraction in the SEM, *Mater. Charact.* 139 (2018) 452–462, <https://doi.org/10.1016/j.matchar.2018.03.026>.
- [14] S.I. Wright, M.M. Nowell, R. de Kloe, P. Camus, T. Rampton, Electron imaging with an EBSD detector, *Ultramicroscopy* 148 (2015) 132–145, <https://doi.org/10.1016/j.ultramic.2014.10.002>.
- [15] N. Brodusch, H. Demers, R. Gauvin, Dark-field imaging based on post-processed electron backscatter diffraction patterns of bulk crystalline materials in a scanning electron microscope, *Ultramicroscopy* 148 (2015) 123–131, <https://doi.org/10.1016/j.ultramic.2014.09.005>.
- [16] N. Brodusch, H. Demers, R. Gauvin, N. Brodusch, H. Demers, R. Gauvin, Imaging with a commercial electron backscatter diffraction (EBSD) camera in a scanning electron microscope: a review, *J. Imaging* 4 (7) (2018) 88, <https://doi.org/10.3390/jimaging4070088>.
- [17] N. Brodusch, H. Demers, M. Trudeau, R. Gauvin, Acquisition parameters optimization of a transmission electron forward scatter diffraction system in a cold-field emission scanning electron microscope for nanomaterials characterization, *Scanning* 35 (2013) 375–386, <https://doi.org/10.1002/sca.21078>.
- [18] C. Sun, E. Müller, M. Meffert, D. Gerthsen, On the progress of scanning transmission electron microscopy (STEM) imaging in a scanning electron microscope, *Microsc. Microanal.* 24 (2018) 99–106, <https://doi.org/10.1017/S1431927618000181>.
- [19] K.P. Rice, R.R. Keller, M.P. Stoykovich, Specimen-thickness effects on transmission Kikuchi patterns in the scanning electron microscope, *J. Microsc.* 254 (2014) 129–136, <https://doi.org/10.1111/jmi.12124>.
- [20] S.I. Wright, M.M. Nowell, R. de Kloe, L. Chan, Orientation precision of electron backscatter diffraction measurements near grain boundaries, *Microsc. Microanal.* (2014) 1–12, <https://doi.org/10.1017/S143192761400035X>.
- [21] MICROSCOPE ACCESSORY SOLUTIONS HAADF Annular SEM STEM detector, n.d. https://deben.co.uk/wp-content/uploads/2011/08/DEB3416_DatasheetA4_HAADF-Annular-STEM-Detector_v2-4.pdf (Accessed 21 May 2019).
- [22] S. Zaefferer, A critical review of orientation microscopy in SEM and TEM, *Cryst. Res. Technol.* 46 (2011) 607–628, <https://doi.org/10.1002/crat.201100125>.
- [23] Sample Preparation - DENSolutions, (n.d.). <http://densolutions.com/sample-preparation/> (Accessed 30 November 2017).
- [24] H. Alimadadi, A.B. Fanta, R. Akiyoshi, T. Kasama, A.D. Rollett, M.A.J. Somers, K. Pantleon, Optimal microstructural design for high thermal stability of pure FCC metals based on studying effect of twin boundaries character and network of grain boundaries, *Mater. Des.* (2018) 151, <https://doi.org/10.1016/j.matdes.2018.04.056>.